Research Square

Preprints are preliminary reports that have not undergone peer review.
They should not be considered conclusive, used to inform clinical practice,
or referenced by the media as validated information.

Cellular contractility-guided osteovascular organoids coordinate metabolic reprogramming and lactate shuttling

Longwei Lv

lvlw@bjmu.edu.cn

Peking University School and Hospital of Stomatology

Zhanqi Wang

Peking University https://orcid.org/0000-0002-5907-9134

Zhuqing Wan

Peking University School and Hospital of Stomatology

Dongdong Huang

Peking University School and Hospital of Stomatology

Yicheng Yang

Department of Prosthodontics, Peking University School and Hospital of Stomatology

Jundan Yi

Peking University School and Hospital of Stomatology

Xiaoqiang Bai

Peking University School and Hospital of Stomatology

YangKun Liu

Institute of Medical Technology, Peking University Health Science Center

Mingchu Zhao

Peking University School and Hospital of Stomatology

Xiaodong Guo

Peking University School and Hospital of Stomatology

Yongsheng Zhou

Peking University School and Hospital of Stomatology https://orcid.org/0000-0002-4332-0878

Article

Keywords:

Posted Date: November 13th, 2026

DOI: https://doi.org/10.21203/rs.3.rs-11559522/v1

License: This work is licensed under a Creative Commons Attribution 4.0 International License.
Read Full License

Additional Declarations: There is **NO** Competing Interest.

Title: Cellular contractility-guided osteovascular organoids coordinate metabolic reprogramming and lactate shuttling

Authors: Zhanqi Wang[a,#], Zhuqing Wan[a,#], Dongdong Huang[a], Yicheng Yang[a], Jundan Yi[a], Xiaoqiang Bai[a], Yangkun Liu[a], Mingchu Zhao[a], Xiaodong Guo[a], Yongsheng Zhou[a,*], Longwei Lv[a,b*]

Affiliations:

[a] *Department of Prosthodontics, Peking University School and Hospital of Stomatology & National Center of Stomatology & National Clinical Research Center for Oral Diseases & National Engineering Research Center of Oral Biomaterials and Digital Medical Devices & Beijing Key Laboratory for Intelligent Biomanufacturing and Regeneration of Craniofacial Tissues & Beijing Key Laboratory of Digital Stomatology & NHC Key Laboratory of Digital Stomatology, Beijing 100081, China*

[b] *Peking University Hospital of Stomatology Sanya Division (Sanya Stomatology Center), Hainan Province, Sanya 572013, China*

[#]These authors contributed equally to this work.

***Correspondence should be addressed to:**

Yongsheng Zhou, Ph.D. & D.D.S., Dean and Professor,

Department of Prosthodontics, Peking University School and Hospital of Stomatology, 22 Zhongguancun South Avenue, Beijing, 100081, China.

E-mail address: kqzhouysh@hsc.pku.edu.cn

Longwei Lv, Ph.D., Chair and Professor

Department of Prosthodontics, Peking University School and Hospital of Stomatology, 22 Zhongguancun South Avenue, Beijing, 100081, China.

E-mail address: lvlw@bjmu.edu.cn

Declarations of interest: none

Title: Cellular contractility-guided osteovascular organoids coordinate metabolic reprogramming and lactate shuttling

Abstract

Effective vascularization remains a major challenge in organoid engineering. Current strategies commonly rely on biochemical induction, cellular composition optimization, or exogenous vascular guidance, whereas whether cell-intrinsic mechanics can be harnessed to drive vascularized organoid maturation remains unclear. Here, we establish contractility-guided osteovascular organoids by using hydrogel pore architecture as a simple physical cue to calibrate cellular contractility during three-dimensional maturation. An intermediate-pore microenvironment established a balanced contractility window that maximized spheroid sprouting and coordinated osteogenic-endothelial maturation, yielding functionally mature osteovascular organoids that enhanced bone formation and neovascularization in rat femoral defects. Mechanistically, insufficient contractility limited multicellular organization and endothelial cells (ECs) lactate supply, whereas excessive contractility disrupted junctional organization and impaired mesenchymal stem cells (MSCs) lactate uptake. The optimal contractile state enabled productive EC-to-MSC lactate shuttling by coordinating monocarboxylate transporter 4 (MCT4)-associated lactate export in ECs with MCT1-dependent lactate uptake in MSCs, thereby coupling endothelial glycolysis to osteogenic oxidative metabolism. These findings identify cell-intrinsic contractility as a physical regulator of osteovascular organoid maturation and establish pore-regulated contractility as a simple design principle for engineering functionally mature vascularized bone tissues.

Keywords: Osteovascular organoids; Cellular contractility; Lactate shuttling; Metabolic

coupling; Pore-tunable hydrogel

Introduction

Effective vascularization remains difficult to achieve in osteovascular organoid engineering, limiting their maturation and functional development[1-5]. Current vascularization strategies mainly rely on osteogenic or angiogenic biochemical induction, modulation of cellular composition or organization, and incorporation of exogenous vascular templates[1,4-8]. However, biochemical induction often introduces complex and context-dependent signalling inputs[1,9], cell-organization strategies depend on predefined spatial control and may constrain intrinsic self-organization[9,10], and exogenous vascular templates increase fabrication complexity[11]. Directly tuning the mechanical microenvironment during three-dimensional (3D) culture may therefore provide a more controllable and promising strategy for promoting osteovascular organoid maturation[12-16].

Cellular contractility is a key mechanical regulator during 3D organoid culture. It enables cells to generate actomyosin-based forces and transmit tension across cell-matrix and cell-cell adhesions[13]. Previous studies have established that contractile force regulates cell spreading[17], matrix remodeling[18,19], collective migration[20], and junctional organization[21-23], all of which are critical for tissue morphogenesis[14,24]. In multicellular organoid systems, this force-generating state may have particular importance because organoid maturation requires coordinated cell rearrangement, stable intercellular contacts, and lineage-specific organization rather than isolated single-cell responses[14,15]. Nevertheless, most studies of cellular contractility have

77 focused on two-dimensional substrates[13], single-cell behaviour[25], or simplified tissue models[26].
78 How cellular contractility can be tuned to construct osteovascular organoids in 3D culture, and
79 how it directs coordination between mesenchymal stem cells (MSCs) and endothelial cells (ECs)
80 during osteogenic-endothelial maturation, remain unclear.
81
82 In hydrogel-based 3D culture of osteovascular organoids, cellular contractility is shaped by the
83 physical properties of the surrounding matrix[27-31]. Among these properties, pore structure is a
84 non-negligible matrix feature, as it alters cell-accessible space and physical confinement[32-34],
85 with potential implications for cellular contractility within embedded multicellular constructs.
86 Such pore-regulated contractility may influence not only multicellular organization, but also
87 intercellular communication and metabolic coordination. Lineage-specific metabolic
88 coordination is central to osteovascular organoid maturation, because EC sprouting and
89 angiogenic activation rely heavily on glycolysis[35,36], whereas MSC osteogenic differentiation
90 requires mitochondrial metabolism and biosynthetic activity[37-39]. However, whether pore-
91 regulated cellular contractility coordinates metabolic crosstalk between ECs and MSCs, and
92 how this coupling supports osteovascular organoid maturation, remains unknown.
93
94 Here, we establish contractility-guided osteovascular organoids by embedding MSC/EC
95 spheroids in pore-tunable hydrogel microenvironments. This platform preserves direct
96 mesenchymal-endothelial contact while using pore structure to tune cellular contractility within
97 3D culture. We identify an intermediate-pore microenvironment that generates a balanced
98 cellular contractility window, thereby promoting spheroid sprouting, osteogenic-endothelial

maturation, ectopic ossification, and bone repair. Mechanistically, insufficient EC contractility limits lactate supply, whereas excessive MSC contractility suppresses monocarboxylate transporter 1 (MCT1)-dependent lactate uptake and osteogenic maturation. These findings reveal EC-to-MSC lactate shuttling as a metabolic mechanism underlying the contractility window and define pore-regulated cellular contractility as a physical-metabolic design principle for engineering mature osteovascular organoids and vascularized bone tissues.

Results

2.1. Pore-guided osteovascular organoids achieve coordinated osteogenic and vascular maturation

The porous gelatin methacryloyl (GelMA) hydrogels exhibited progressively larger interconnected pores, with mean pore diameters of 40.8 ± 7.9, 73.5 ± 8.4, and 112.8 ± 10.1 μm in the low-pore (LP), medium-pore (MP), and high-pore (HP) groups, respectively, whereas non-porous (NP) hydrogels lacked detectable interconnected pores (Supplementary Fig. 1a-c). Compared with NP hydrogels, LP, MP, and HP hydrogels exhibited lower stiffness, while maintaining broadly comparable rheological profiles and mechanical moduli among the porous groups (Supplementary Fig. 1d-f). Larger pore dimensions were associated with increased swelling and degradation, indicating pore-dependent changes in hydrogel hydration and degradability (Supplementary Fig. 1g, h). FITC-dextran fluorescence intensity and permeability rate also increased with pore enlargement, indicating enhanced matrix transport and molecular accessibility within the porous network (Supplementary Fig. 1i, j). Thus, this porous GelMA platform enabled modulation of cell-accessible space and molecular transport under broadly

comparable mechanical conditions among the porous groups.

To examine how pore-tunable hydrogels influence osteovascular organoid maturation, mCherry-labelled human bone marrow-derived MSCs (hBMSCs) and EGFP-labelled human umbilical vein ECs (HUVECs) were assembled into composite osteovascular spheroids and encapsulated within the NP, LP, MP, or HP hydrogels. The NP group showed restricted cell spreading and more dead-cell signals, consistent with limited cell-accessible space and solute transport in the non-porous matrix (Supplementary Fig. 2a). Among the porous groups, the MP group exhibited the most robust sprouting at days 3 and 7, with greater invasion distance, branch point number, sprout number, and filopodia length than the LP or HP groups (Supplementary Fig. 2b, c).

Organoids formed under different pore conditions were then evaluated for ectopic bone-like tissue formation and self-mineralization in nude mice (Fig. 1a). The MP group generated more extensive mineralized tissue, with higher bone mineral density (BMD), bone volume fraction (BV/TV), and trabecular number (Tb.N) than the LP or HP groups (Fig. 1b). The MP group also exhibited the most pronounced vascularized tissue appearance, bone-like tissue organization, and mineral deposition (Fig. 1c, d). The MP group further exhibited stronger OCN signals, together with more evident CD31/α-SMA-positive vascular-associated structures, indicating enhanced osteogenic and vascular-associated tissue formation (Fig. 1e).

The intermediate-pore microenvironment also promoted osteogenic-endothelial maturation *in*

vitro. The MP group exhibited stronger RUNX2 and CD31 fluorescence than the LP and HP groups, along with increased gene expression of *RUNX2*, *OCN*, *PECAM1*, and *VEGFA* (Fig. 1f-h). Notably, the MP group also exhibited increased PDGFR-β and APLN expression, suggesting that the intermediate-pore microenvironment may support pericyte-like supportive phenotypes in hBMSCs and tip-cell-associated activation in HUVECs (Fig. 1i-l). Additionally, the 1:1 hBMSC:HUVEC ratio produced the most favorable sprouting profile within the MP group, while maintaining balanced RUNX2 and CD31 expression compared with 3:1 or 1:3 spheroids (Supplementary Fig. 3a, b), thereby supporting the cell-composition strategy used for organoid assembly. Together, these findings indicate that an intermediate pore architecture provides a favourable structural window to coordinate early sprouting, cellular co-maturation, and in vivo ectopic osteogenic function of osteovascular organoids.

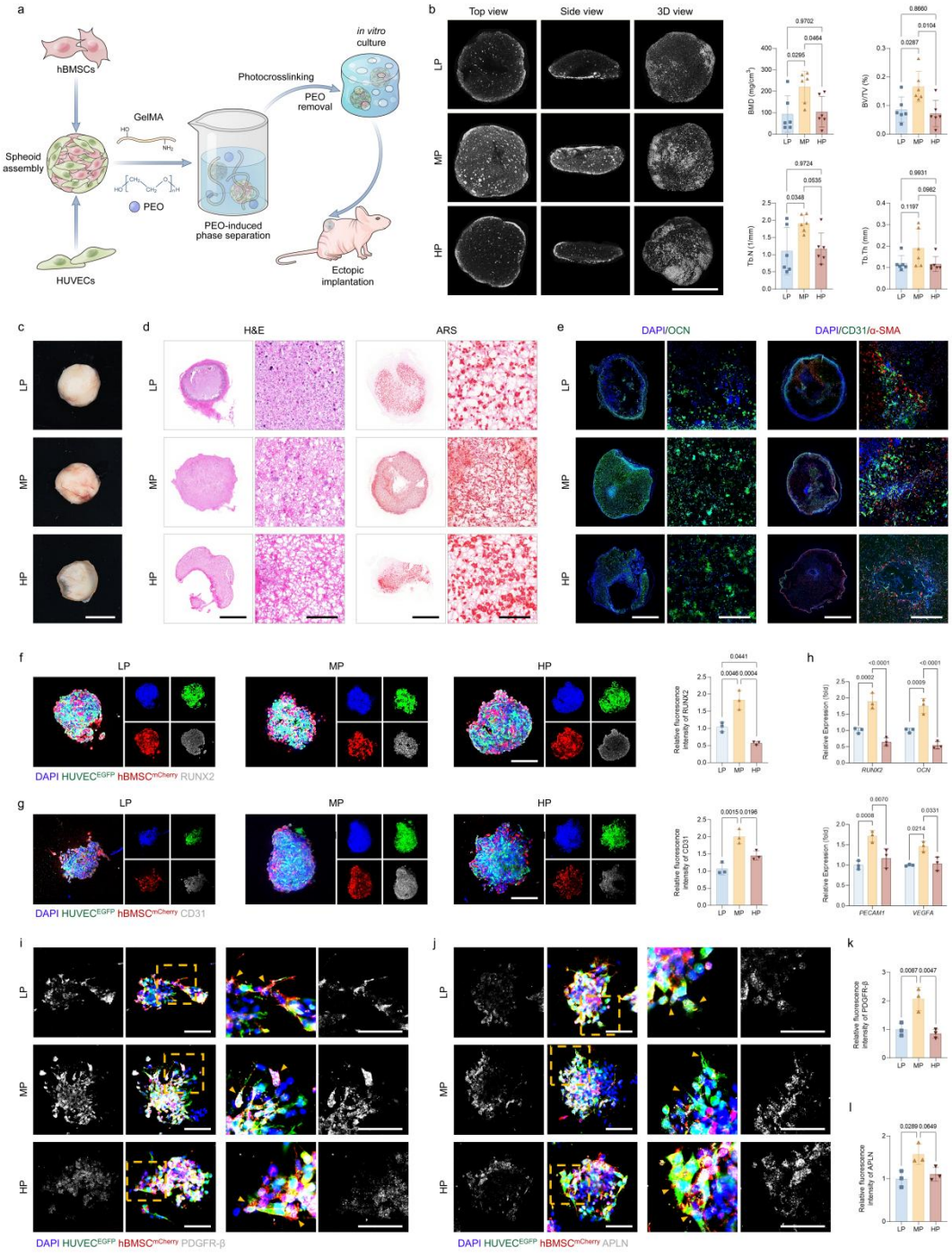


Fig. 1 | Pore-tunable hydrogels enable osteovascular organoid maturation

a, Schematic illustration of pore-tunable hydrogel fabrication and hBMSC/HUVEC osteovascular organoid generation. **b,** Representative micro-CT reconstructions of explanted osteovascular organoid constructs generated from LP, MP, and HP groups, with quantification of BMD, BV/TV, Tb.N, and Tb.Th (n = 6). **c,** Gross images of explanted osteovascular organoid

constructs from different groups. **d,** H&E staining and Alizarin Red S staining of explanted osteovascular organoid constructs. **e,** Representative OCN and CD31/α-SMA immunofluorescence staining of explanted osteovascular organoid constructs. **f,** Representative RUNX2 immunofluorescence staining of LP, MP, and HP groups cultured *in vitro* with quantification of fluorescence intensity (n = 3). **g,** Representative CD31 immunofluorescence staining of different groups, with quantification of fluorescence intensity (n = 3). **h,** qPCR analyses of *RUNX2*, *OCN*, *PECAM1*, and *VEGFA* of different groups (n = 3). **i,** Representative PDGFR-β immunofluorescence staining of different groups and (**k**) quantification of fluorescence intensity (n = 3). **j,** Representative APLN immunofluorescence staining of different groups and (**l**) quantification of fluorescence intensity (n = 3). Yellow boxes indicate regions shown at higher magnification. Yellow arrowheads indicate representative PDGFR-β-positive hBMSCs in (**i**) and APLN-positive HUVECs in (**j**). Data are presented as mean ± SD. Scale bars, 5 mm for (**b**, **c**), 3 mm for low-magnification images in (**d**, **e**), 200 μm for high-magnification images in (**d, e**), 100 μm for (**f**, **g**, **i, j**). One-way ANOVA followed by Tukey's post-hoc test for multiple comparisons was applied. Exact P values and sample sizes (n) are provided.

2.2. A pore-mediated intermediate contractility window regulates cell-cell junctions and osteovascular function

To further elucidate the mechanisms underlying enhanced osteogenic and endothelial maturation in the MP group, we performed transcriptomic analysis, implicating the contractility-associated programme as a key regulatory feature. The MP group showed concurrent

upregulation of osteogenic and angiogenic genes, together with enrichment of osteogenic-endothelial maturation-related pathways (Supplementary Fig. 4a-d). Notably, genes associated with mechanotransduction, actin cytoskeletal organization and cellular contractility, including *YAP1*, *MYL9*, *TLN1* and *RHOA*, increased with pore enlargement, whereas cell-cell junction-associated genes, including *CDH2*, *CDH5* and *CTNNB1*, were more highly expressed in the MP group (Fig. 2a). Consistently, the MP group was enriched for focal adhesion, collagen-containing extracellular matrix and regulation of actin cytoskeleton organization relative to the LP group (Fig. 2b). Compared with the HP group, the MP group showed stronger enrichment of cell-cell junction-related terms, whereas the HP group retained stronger contractility-associated signatures (Fig. 2c). These transcriptomic differences indicate that the intermediate-pore microenvironment did not simply enhance osteogenic and endothelial maturation, but established a contractility-associated state coupled to junctional organization across the co-cultured lineages.

To investigate whether pore-regulated cellular contractility was required for osteovascular organoid maturation, we examined contractile activity and junctional organization across the pore groups and after pharmacological perturbation. Membrane tension and p-MLC2 levels progressively increased from LP to HP groups, consistent with a pore-dependent increase in the cellular contractile state (Fig. 2d, e). In contrast, intercellular junctional organization did not increase in parallel with contractility. N-cadherin and β-catenin signals peaked in the MP group but declined in the HP group (Fig. 2f, g), suggesting that junction integrity depends on a balanced contractile state rather than maximal tension (Fig. 2h). Reducing contractility with the

ROCK inhibitor Y-27632 weakened the junction-associated markers in the MP group, yet partially restored the impaired junctional signals in the HP group (Fig. 2d-g). Consistent with this bidirectional response, either Y-27632-mediated inhibition or calyculin A (CA)-mediated enhancement of contractility in the MP group reduced N-cadherin and β-catenin signals, together with RUNX2 and CD31 expression (Fig. 2i and Supplementary Fig. 4e).

Meanwhile, HUVEC-only spheroids reproduced this pore-dependent contractility-junction relationship. CD31 expression was highest in the MP group, whereas membrane tension, p-MLC2, and contractility-related genes increased with pore size (Supplementary Fig. 5a-d). Endothelial junction markers, including VE-cadherin and β-catenin, peaked in the MP group and declined in the HP group (Supplementary Fig. 5e, f). These findings indicate that pore-regulated cellular contractility controls osteovascular organoid maturation through a non-linear contractility window. An intermediate contractile state favored osteovascular organization and stable junction formation, whereas either insufficient or excessive contractility compromised junction integrity and osteovascular function.

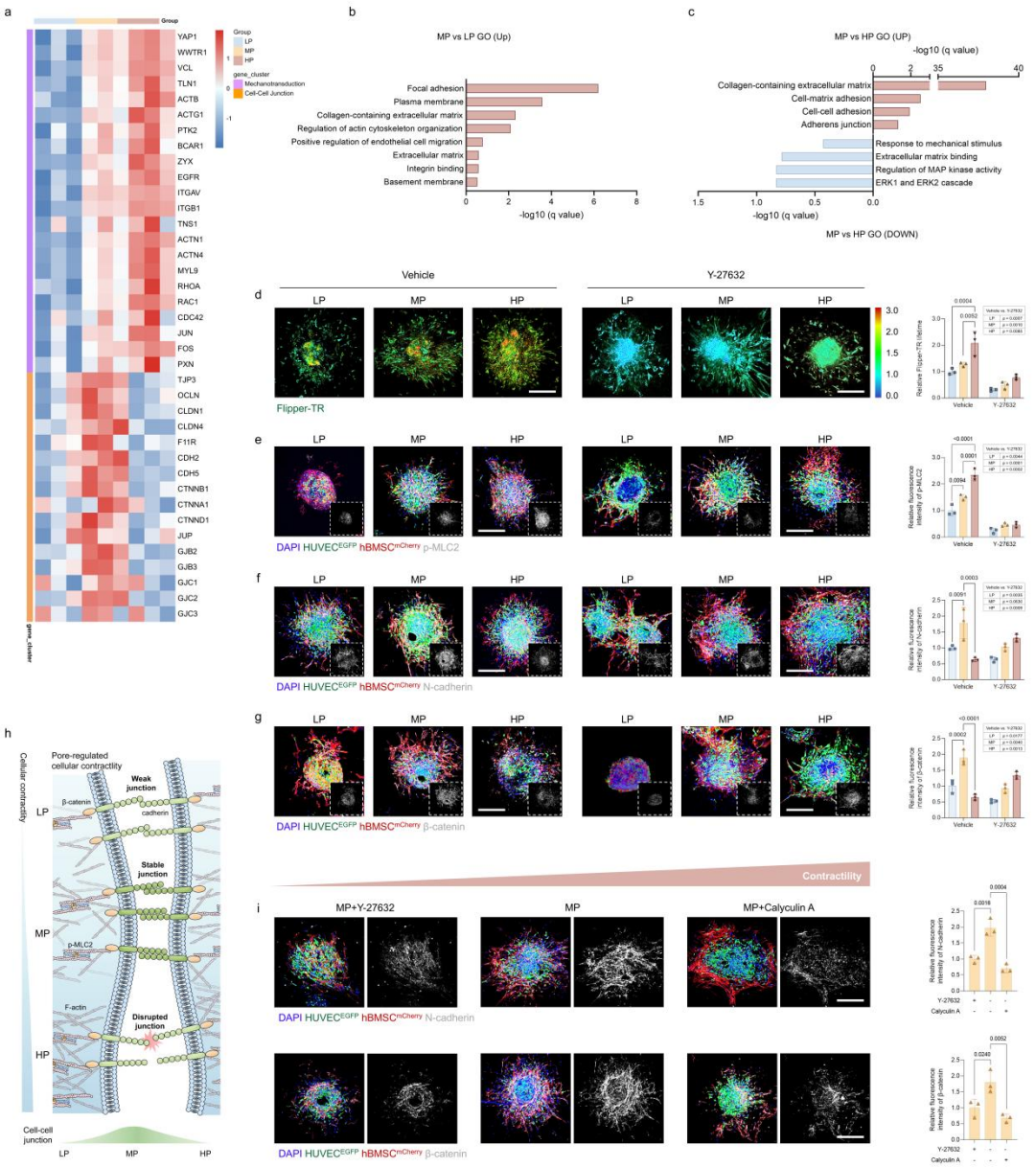


Fig. 2 | Pore-regulated contractility shapes junctional organization

a, Heatmap of mechanotransduction- and cell-cell junction-related genes in the LP, MP, and HP groups. **b,** GO enrichment analysis of upregulated terms enriched in MP vs. LP groups. **c,** GO enrichment analysis of terms enriched in MP vs. HP groups. **d,** Representative Flipper-TR images of LP, MP, and HP groups treated with vehicle or Y-27632, with quantification of membrane tension (n = 3). **e-g,** Representative immunofluorescence staining and corresponding quantification of p-MLC2 (**e**), N-cadherin (**f**) and β-catenin (**g**) in the indicated

treatment groups (*n* = 3). **h,** Schematic illustration of the relationship between cellular contractility and cell-cell junction. **i,** Representative N-cadherin and β-catenin immunofluorescence staining and quantification in the MP group treated with vehicle, Y-27632, or calyculin A (*n* = 3). Data are presented as mean ± SD. Scale bars, 100 μm for (**d-g**, **i**). For Fig. **d-g**, two-sided Student's *t*-test was used to compare Vehicle and Y-27632 treatment within the LP, MP, and HP groups. One-way ANOVA followed by Tukey's post-hoc test for multiple comparisons was applied for the others. Exact *P* values and sample sizes (*n*) are provided.

2.3. Cellular contractility is associated with lineage-specific metabolic reprogramming

Given that pore-associated contractility and junctional states were associated with enhanced osteovascular organoid maturation, we next performed metabolomic profiling to determine whether these mechanically regulated states were accompanied by metabolic reprogramming during organoid maturation. The MP group showed coordinated activation of glycolysis- and oxidative phosphorylation-associated programs, whereas the HP group retained glycolytic features but showed weaker oxidative phosphorylation signatures (Fig. 3a, c). Consistently, oxidative phosphorylation-associated genes, including *COX4I1* and *ATP5A1*, and glycolysis-associated genes, including *SLC2A1* and *HK2*, were more highly expressed in the MP group (Fig. 3b). The MP group also exhibited higher levels of representative glycolytic and tricarboxylic acid (TCA) cycle metabolites, including 3-phosphoglycerate, pyruvate, L-lactate, 2-ketoglutarate, and succinate (Fig. 3d, e). Integrated transcriptomic and metabolomic patterns further linked intermediate-pore osteogenic-endothelial maturation to metabolic pathway changes (Supplementary Fig. 6a).

The metabolic state of the MP group was functionally linked to osteogenic-endothelial maturation. Because endothelial sprouting and angiogenic activation rely heavily on glycolytic metabolism[35], whereas osteogenic differentiation requires mitochondrial oxidative metabolism[40], metabolic inhibition was used to test the contribution of these pathways in the MP group. Inhibition of glycolysis with 2-deoxy-D-glucose (2-DG) markedly reduced CD31 signals and also decreased RUNX2 expression, whereas inhibition of mitochondrial oxidative phosphorylation with oligomycin caused a more pronounced reduction in RUNX2 while also suppressing CD31 (Fig. 3f). These results suggest that dual-lineage maturation of osteovascular organoids requires coordinated support from glycolytic and mitochondrial metabolism.

The contractility-associated metabolic remodeling was further resolved at the lineage level by metabolic flux analysis of sorted HUVECs and hBMSCs. In sorted hBMSCs, the MP group exhibited higher basal respiration, maximal respiration, and spare respiratory capacity than the LP and HP groups, indicating enhanced oxidative phosphorylation capacity (Fig. 3g, h and Supplementary Fig. 6b). In sorted HUVECs, both the MP and HP groups displayed higher glycolysis, glycolytic capacity, and glycolytic reserve than the LP group (Fig. 3i). Thus, the MP group was distinguished by an intermediate contractile state that simultaneously maintained HUVEC glycolytic activity and hBMSC oxidative respiration. Under the MP condition, reducing contractility with Y-27632 decreased hBMSC mitochondrial respiration and altered HUVEC glycolytic parameters. Enhancing contractility with calyculin A produced a similar loss of hBMSC oxidative respiration (Supplementary Fig. 6c). Together, these findings indicate that appropriate

cellular contractility was associated not only with structural organization but also with lineage-specific metabolic reprogramming within osteovascular organoids.

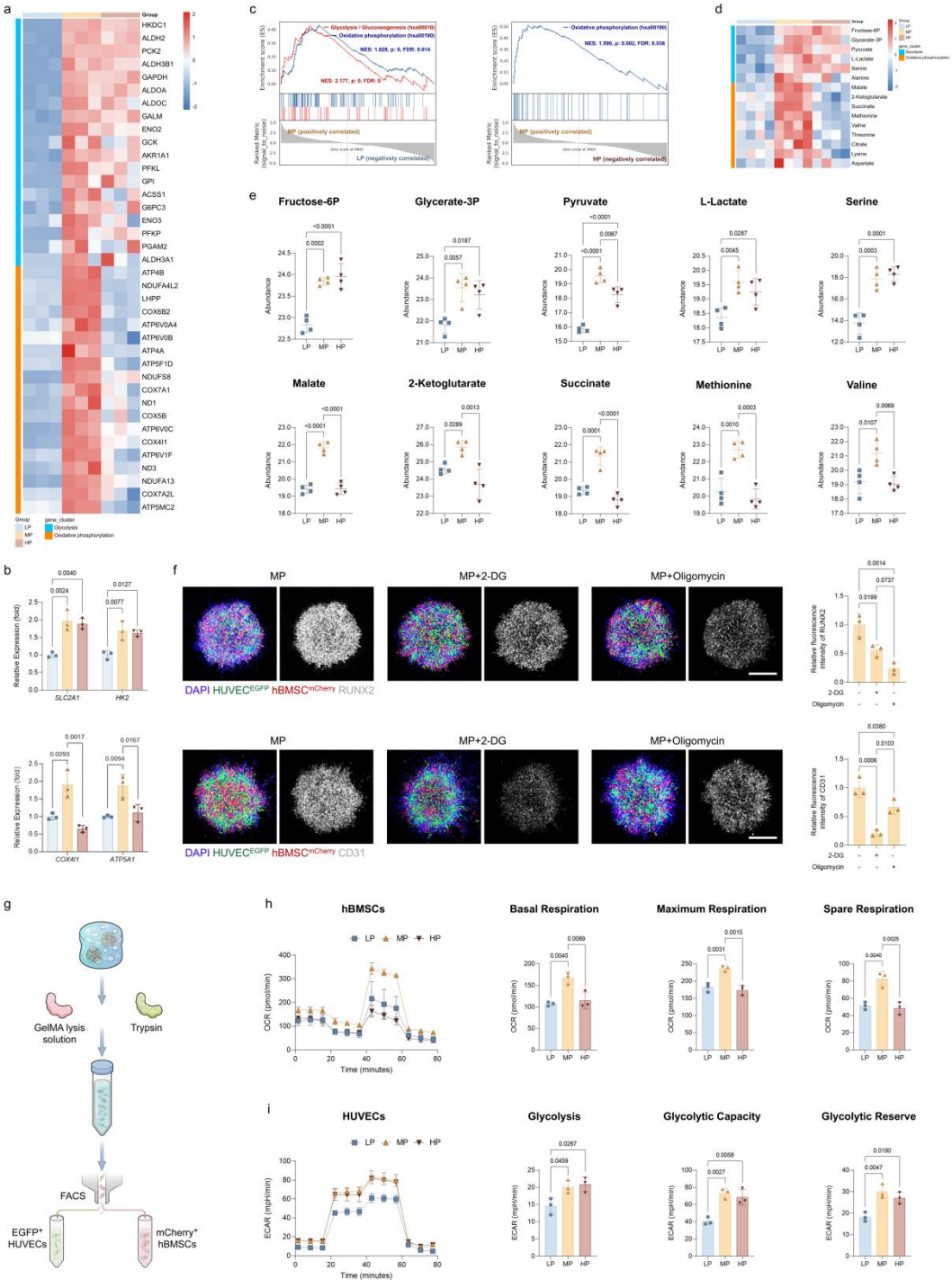


Fig. 3 | Contractile states coincide with lineage-specific metabolic remodeling

a, Heatmap of glycolysis- and oxidative phosphorylation-related genes in the LP, MP, and HP groups. **b,** qPCR analyses of *COX4I1*, *ATP5A1*, *GLUT1*, and *HK2* in different groups (n = 3). **c,**

GSEA showing enrichment of Glycolysis/Gluconeogenesis and Oxidative phosphorylation in MP vs. LP and MP vs. HP groups. **d,** Heatmap of differential metabolites associated with glycolysis and oxidative phosphorylation in the LP, MP, and HP groups. **e,** Quantification of representative glycolytic and TCA-cycle-related metabolites, including glycerate-3P, pyruvate, L-lactate, 2-ketoglutarate, and succinate (*n* = 4). **f,** Representative RUNX2 and CD31 immunofluorescence staining and quantification in the MP group after 2-DG or oligomycin treatment (*n* = 3). **g,** Schematic illustration of fluorescence-activated cell sorting for lineage-specific metabolic flux analysis. **h,** Seahorse OCR analysis of sorted hBMSCs, with quantification of basal respiration, maximal respiration, and spare respiratory capacity (*n* = 3). **i,** Seahorse ECAR analysis of sorted HUVECs, with quantification of glycolysis, glycolytic capacity, and glycolytic reserve (*n* = 3). Data are presented as mean ± SD. Scale bars, 100 μm for (**f**). One-way ANOVA followed by Tukey's post-hoc test for multiple comparisons was applied. Exact *P* values and sample sizes (*n*) are provided.

2.4. HUVEC-to-hBMSC lactate shuttling mediates metabolic coupling within the contractility window

Intriguingly, increased cellular contractility was accompanied by reduced oxidative metabolism while glycolytic features were preserved. Compared with the MP group, the HP group retained relatively high levels of glycolytic intermediates and L-lactate, but showed lower tricarboxylic acid (TCA) cycle-associated metabolites (Fig. 3d, e). Because lactate is a glycolysis-derived intermediate that can be transferred between cells and used to support oxidative metabolism[41,42], this pattern suggested that excessive cellular contractility did not primarily

299 restrict lactate generation, but may have impaired lactate uptake or downstream utilization by
300 hBMSCs. We therefore further examined whether lactate shuttling mediated metabolic coupling
301 under the contractility window.
302
303 Consistent with the metabolic preference of glycolytic HUVECs and oxidative hBMSCs, lactate
304 transport showed a contractility-dependent donor-recipient pattern. Extracellular L-lactate
305 levels increased over time and were higher in the MP and HP groups than in the LP group,
306 indicating enhanced lactate availability under intermediate- and high-contractility conditions
307 (Fig. 4a). However, intracellular lactate responses in hBMSCs, reflected by the Laconic-NLS
308 mTFP/mVenus fluorescence resonance energy transfer (FRET) ratio, were highest in the MP
309 group but markedly reduced in the LP and HP groups (Fig. 4b). This divergence suggested that
310 the HP group retained lactate output but failed to support efficient hBMSC lactate uptake.
311 Consistently, MCT4, which preferentially supports lactate efflux from glycolytic cells[43], was more
312 highly expressed in HUVECs in the MP and HP groups than in the LP group, supporting
313 enhanced endothelial lactate export as contractility increased (Fig. 4c). By contrast, MCT1,
314 which is commonly associated with lactate uptake and oxidative utilization[44], was most strongly
315 expressed in hBMSCs in the MP group but decreased in the LP and HP groups, as reflected
316 by both fluorescence intensity and the proportion of MCT1-positive hBMSCs (Fig. 4d). In
317 hBMSC-only spheroids, Laconic-NLS FRET ratio and lactate levels remained comparable
318 among the pore groups (Supplementary Fig. 7a, b), supporting the interpretation that the
319 enhanced lactate response in hBMSCs arose from mesenchymal–endothelial interactions
320 rather than from a direct pore effect on hBMSCs alone. Under the MP condition, Y-27632

reduced MCT4 expression in HUVECs, whereas calyculin A decreased MCT1 expression in hBMSCs (Supplementary Fig. 7c). Both insufficient and excessive contractility reduced the Laconic-NLS FRET ratio in hBMSCs, and calyculin A further increased extracellular L-lactate levels (Supplementary Fig. 7d, e), supporting the interpretation that excessive contractility impaired lactate uptake rather than lactate availability.

Cell type-specific perturbation of contractility showed that productive lactate shuttling required both endothelial lactate supply and hBMSC lactate uptake. *MYL9* knockdown reduced p-MLC2 signals in HUVECs, accompanied by decreased HUVEC MCT4 expression and lower extracellular lactate levels (Fig. 4e, f and Supplementary Fig. 8a). Accordingly, the hBMSC Laconic-NLS FRET ratio and RUNX2 expression decreased (Fig. 4g). Exogenous lactate supplementation partially restored the hBMSC lactate response and RUNX2 expression (Fig. 4h), indicating that reduced HUVEC contractility restricted hBMSC osteogenic maturation primarily by limiting lactate supply. Conversely, phosphomimetic MLC2 (T18D/S19D) overexpression (OE) increased p-MLC2 signals in hBMSCs but reduced MCT1 expression (Fig. 4i and Supplementary Fig. 8b). Despite increased extracellular lactate levels, the Laconic FRET ratio decreased, and RUNX2 expression was suppressed (Fig. 4j, k). Further lactate supplementation failed to effectively restore RUNX2 expression (Fig. 4l), suggesting that under excessive hBMSC contractility, the limiting factor was not lactate supply but impaired MCT1-associated lactate uptake.

Together, these findings indicate that productive HUVEC-to-hBMSC lactate shuttling required

two coordinated conditions: HUVECs maintained lactate production and export, while hBMSCs preserved lactate uptake and response. In the LP group, insufficient cellular contractility limited HUVEC lactate supply, thereby reducing lactate availability for hBMSCs. In contrast, the HP group retained lactate production or export capacity under excessive contractility, but reduced hBMSC MCT1 expression and lactate uptake impaired downstream lactate utilization. Thus, the MP group achieved a balanced contractile state that simultaneously supported endothelial lactate supply and hBMSC lactate uptake, providing a metabolic coupling mechanism that linked the contractility window to osteovascular organoid maturation.

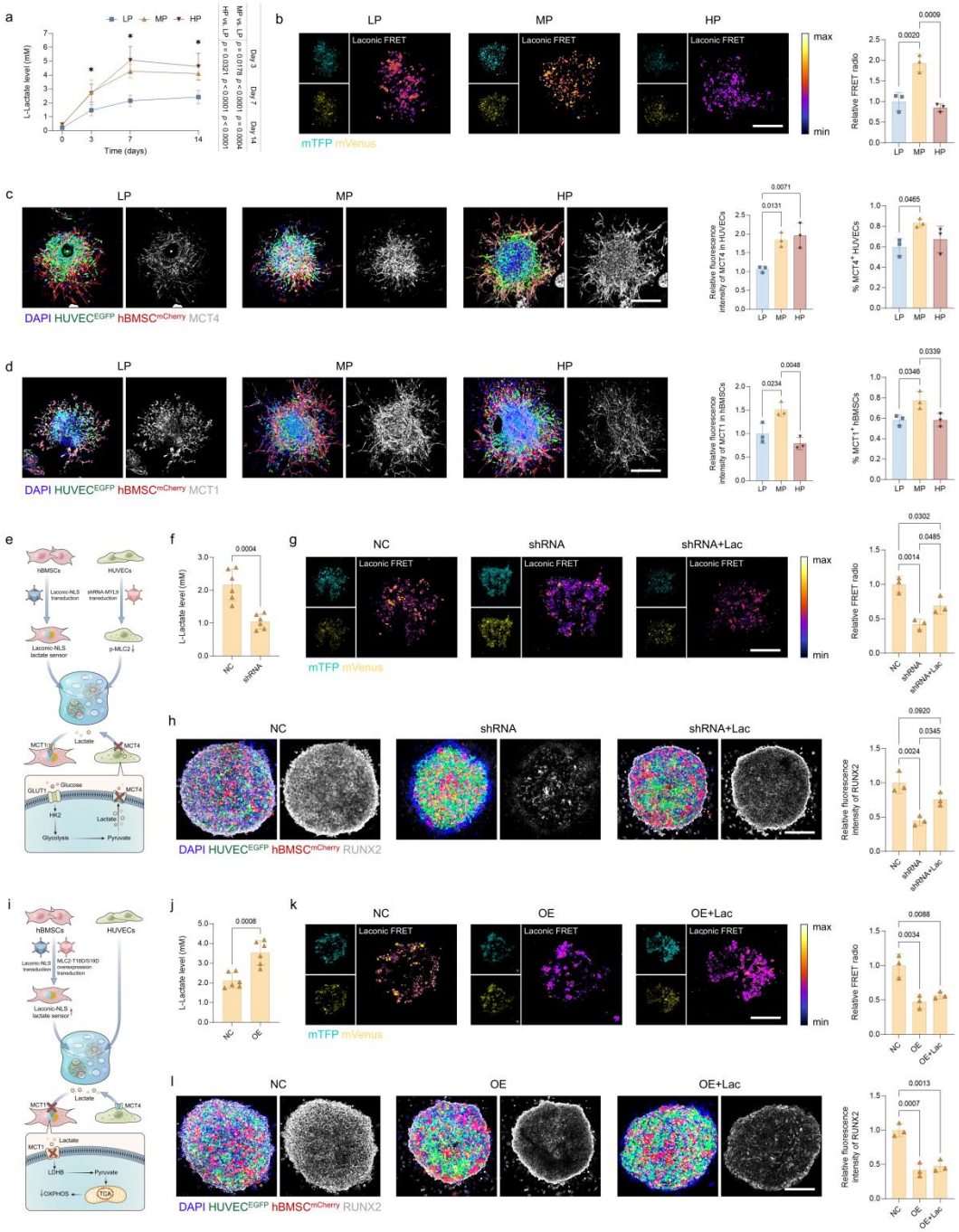


Fig. 4 | Lactate shuttling couples contractility to osteovascular organoid maturation

a, Extracellular L-lactate levels in the LP, MP, and HP groups over time (*n* = 6). **b,** Representative Laconic-NLS imaging in hBMSCs, with FRET ratio quantification of intracellular lactate levels (*n* = 3). **c,** Representative MCT4 immunofluorescence staining in HUVECs, with quantification of fluorescence intensity and the proportion of MCT4-positive HUVECs (*n* = 3).

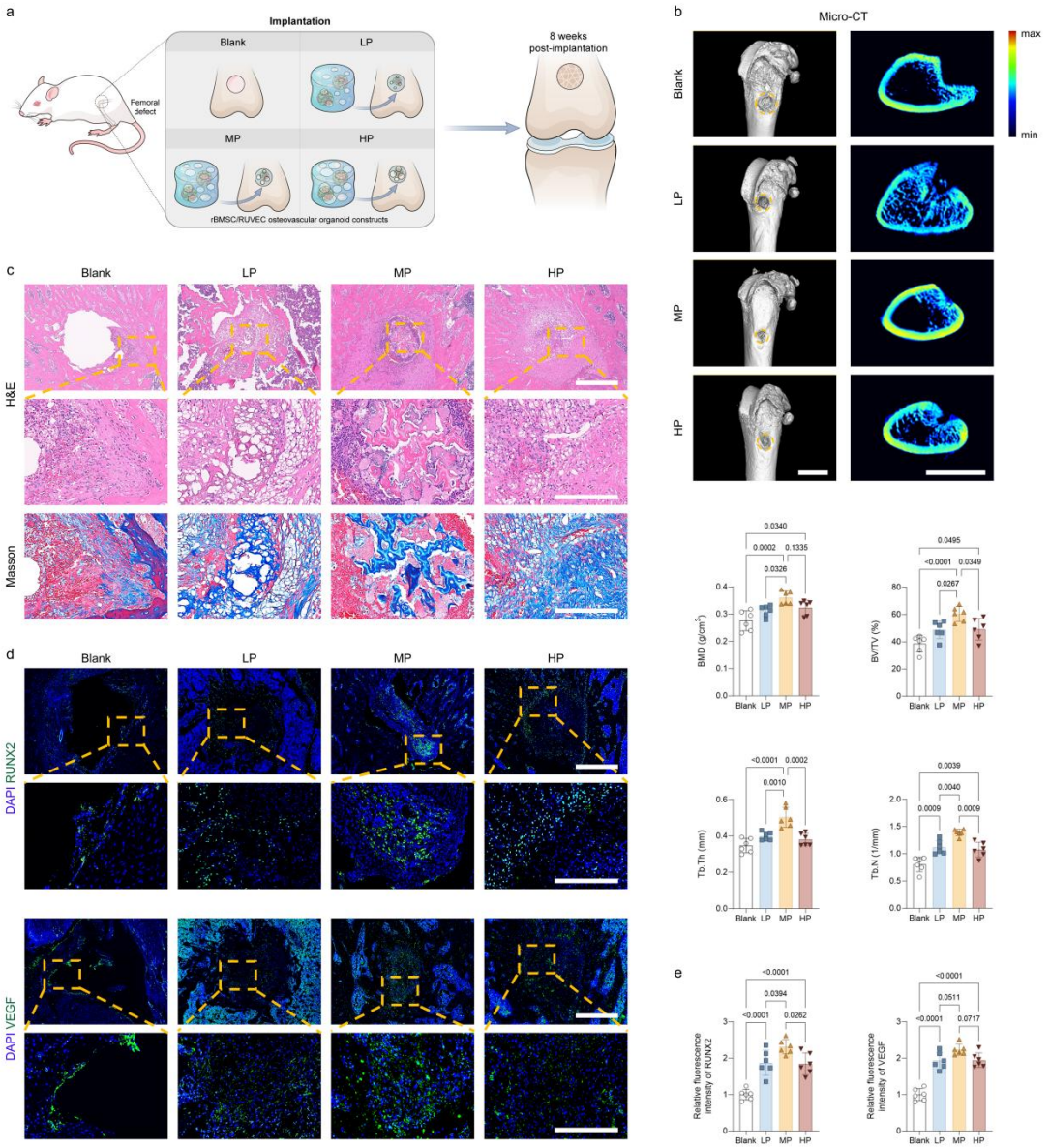
d, Representative MCT1 immunofluorescence staining in hBMSCs, with quantification of fluorescence intensity and the proportion of MCT1-positive hBMSCs (*n* = 3). **e,** Schematic illustration of MYL9 knockdown in HUVECs combined with Laconic-NLS transduction in hBMSCs. **f,** Extracellular L-lactate levels after shRNA-MYL9 (shRNA) transduction (*n* = 6). **g,** Representative Laconic-NLS imaging and FRET ratio quantification after negative control (NC) or shRNA transduction with or without lactate supplementation (*n* = 3). **h,** Representative RUNX2 immunofluorescence staining and quantification in the MP group under different treatments (*n* = 3). **i,** Schematic illustration of phosphomimetic MLC2 (T18D/S19D) overexpression (OE) combined with Laconic-NLS transduction in hBMSCs. **j,** Extracellular L-lactate levels after OE transduction (*n* = 6). **k,** Representative Laconic-NLS imaging and FRET ratio quantification after NC or OE transduction with or without lactate supplementation (*n* = 3). **l,** Representative RUNX2 immunofluorescence staining and quantification in the MP group under different treatments (*n* = 3). Data are presented as mean ± SD. Scale bars, 100 μm for (**b**-**d**, **g**, **h, k**, **l**). Two-sided Student's *t*-test was applied for (**f**, **j**). One-way ANOVA followed by Tukey's post-hoc test for multiple comparisons was applied for the others. For Fig. **a**, * indicates significant differences of both MP and HP groups versus LP group at the corresponding time point. Exact *P* values and sample sizes (*n*) are provided.

2.5. Osteovascular organoids promote repair of rat femoral defects

To determine whether contractility-regulated osteovascular organoids could enhance bone repair, the constructs were assessed in a rat femoral defect model. Species-matched rat osteovascular organoid constructs were generated before implantation into femoral defects (Fig.

5a). The MP group showed more extensive new bone formation and a more continuous trabecular-like architecture within the defect region than the Blank, LP, and HP groups. Quantitative micro-CT analysis further showed higher BV/TV, BMD, trabecular thickness (Tb.Th), and trabecular number (Tb.N) in the MP group (Fig. 5b), indicating enhanced bone regeneration.

Histological and immunostaining features further supported the enhanced repair response in the MP group. The Blank group retained persistent voids and limited tissue repair, the LP group showed modest tissue ingrowth, and the HP group showed partial but less continuous repair, whereas the MP group showed more complete tissue filling and more evident bone-like tissue formation. Collagen deposition was denser in the MP group, suggesting enhanced matrix formation and tissue remodeling (Fig. 5c). The MP group also exhibited stronger RUNX2 and VEGF signals in the defect region, indicating increased local osteogenic activity and vascular-associated responses (Fig. 5d, e). OCN-positive mature osteogenic signal was stronger in the MP group (Supplementary Fig. 9a). No overt histopathological abnormalities were observed in the major organs, providing preliminary evidence of tissue-level biocompatibility of these organoid constructs (Supplementary Fig. 9b). Together, these results demonstrate that MP-induced osteovascular organoids enhanced bone repair in a rat femoral defect model.



397

398 **Fig. 5 | Intermediate-pore osteovascular organoids improve femoral defect repair**

399 **a,** Schematic illustration of osteovascular organoid implantation into rat femoral defects. **b**,

400 Representative micro-CT 3D reconstructions of rat femoral defects in Blank, LP, MP, and HP

401 groups, with quantification of BMD, BV/TV, Tb.N, and Tb.Th (*n* = 6). Yellow outlines indicate the

402 defect regions. **c**, Representative H&E and Masson staining of regenerated tissue within the

403 defect region of different groups. **d,** Representative RUNX2 and VEGF immunofluorescence

404 staining and (**e**) quantification within the defect region of different groups (*n* = 6). Yellow boxes

indicate regions shown at higher magnification. Data are presented as mean ± SD. Scale bars, 4 mm for (**b**), 500 μm for low-magnification images in (**c, d**), 300 μm for high-magnification images in (**c, d**). One-way ANOVA followed by Tukey's post-hoc test for multiple comparisons was used. Exact *P* values and sample sizes (*n*) are provided.

Discussion

In this study, we identify cellular contractility as a central regulator linking matrix architecture to structural and metabolic maturation of osteovascular organoids. An intermediate-pore microenvironment most effectively promoted spheroid sprouting, osteogenic-endothelial maturation, ectopic mineralization, and femoral defect repair. This advantage depended on a balanced cellular contractility window, in which insufficient contractility limited collective organization and endothelial lactate supply, whereas excessive contractility weakened junctional organization and impaired MSC lactate uptake. Mechanistically, the optimal contractile state coordinated lineage-specific metabolism by matching EC glycolytic lactate export with MSC lactate uptake and oxidative utilization. Together, these findings suggest that osteovascular organoid maturation depends not only on matrix permissiveness, but also on a contractile state that coordinates multicellular organization, lineage-specific metabolic reprogramming, and EC-to-MSC lactate shuttling.

Matrix-embedded MSC/EC spheroids provided a useful model for examining pore-dependent multicellular behaviour in osteovascular organoids[4,8,45]. By preserving direct mesenchymal-endothelial contact and local paracrine or metabolic exchange, this format allowed collective

outgrowth and vessel-like morphogenesis to be studied in a 3D hydrogel microenvironment[6,7,46,47]. Thus, compared with dispersed single-cell encapsulation, the spheroid-based design aimed to preserve direct mesenchymal–endothelial contact and multicellular organization for bone-vascular crosstalk.

Balanced cellular contractility appears to be a key mechanical condition for osteovascular organoid organization. Contractile forces are closely coupled to cell adhesion, because actomyosin-generated tension is transmitted through cell-matrix and cell-cell adhesive structures. Previous studies have shown that appropriate mechanical loading can reinforce cadherin-based adhesions and promote junction growth, whereas excessive contractility can destabilize junctional integrity by increasing cadherin bond dissociation[16,21-24,28,48]. This force-adhesion balance is particularly relevant to organoid maturation, where mechanical force and cytoskeletal contractility can actively guide organoid growth, patterning, and morphogenesis, rather than serving only as downstream responses to matrix cues[14,15]. Consistent with this framework, our study establishes a contractility-regulated osteovascular organoid model by tuning hydrogel pore structure as an upstream matrix cue. In this system, pore enlargement progressively increased membrane tension and p-MLC2, but junction-associated markers peaked in the MP group and declined in the HP group. Pharmacological reduction or enhancement of contractility further impaired junctional organization and osteovascular function. Thus, the MP group supported osteovascular organoid maturation by establishing an appropriate contractility window that coordinated adhesive organization, multicellular force transmission, and lineage co-maturation, rather than by maximizing pore permissiveness alone.

Beyond junctional organization, our data indicate that the contractility window is coupled to lineage-specific metabolic remodeling. The central finding is not a global increase in metabolic activity, but coordinated metabolic partitioning between endothelial and osteogenic compartments during osteovascular maturation. Mechanical cues have been increasingly recognized as regulators of metabolic flux, mitochondrial activity, and cell fate, supporting the concept that matrix mechanics can shape metabolic state[49-51]. This concept is particularly relevant in osteovascular organoids, because EC sprouting and angiogenic activation depend strongly on glycolytic metabolism, whereas MSC osteogenic differentiation is closely linked to mitochondrial respiration, redox balance, and biosynthetic activity required for matrix production and mineral-associated maturation[35,40]. Consistent with this requirement for metabolic partitioning, the MP group showed coordinated activation of glycolysis- and oxidative phosphorylation-related programs, and flow-sorted Seahorse analysis further revealed simultaneous maintenance of HUVEC glycolytic activity and hBMSC oxidative respiration. By contrast, the HP group retained relatively high endothelial glycolytic capacity but failed to sustain hBMSC mitochondrial respiration. These findings indicate that excessive pore-associated contractility did not suppress all metabolic activity, but disrupted lineage-level metabolic coordination. Thus, the advantage of the MP group appears to reflect metabolic alignment between endothelial and osteogenic lineages, rather than nonspecific metabolic enhancement.

Lactate may provide a mechanistic link between lineage-specific metabolic alignment and

intercellular communication in osteovascular organoids. Although once regarded mainly as a glycolytic by-product, lactate is now recognized as a transferable metabolite that can regulate cell state and tissue crosstalk[41,42,52,53]. In bone, endothelial-derived lactate has been shown to promote BMSC osteogenic differentiation through histone lactylation, indicating that lactate can act as a metabolic signal linking vascular metabolism to osteogenesis[54]. Genetically encoded Laconic imaging has provided evidence for lactate gradients between glycolytic donor cells and oxidative recipient cells, supporting the role of compartmentalized lactate levels in carrier-mediated metabolic transfer[55]. Similar MCT1-dependent endothelial-to-neuronal lactate shuttling has been reported to promote axonal regeneration after spinal cord injury[56]. Therefore, lactate shuttling is not simply a consequence of extracellular lactate accumulation, but a directional exchange process determined by donor-cell metabolism, transporter expression, and recipient-cell utilization[57-59]. In our osteovascular organoids, glycolytic ECs and oxidative MSCs formed a potential donor-recipient pair. The LP group was mainly limited by insufficient endothelial contractility, which reduced MCT4-associated lactate export and constrained MSC lactate availability. By contrast, the HP group retained lactate production or export capacity, but excessive MSC contractility reduced MCT1-associated lactate uptake and impaired downstream lactate utilization. In summary, the MP group satisfied both conditions, suggesting that productive lactate shuttling requires matched donor-side export and recipient-side uptake rather than high lactate production alone.

The preserved advantage of the MP group across in vitro maturation and in vivo repair supports the broader relevance of balanced cellular contractility in osteovascular organoid engineering.

Nevertheless, bone repair was not complete within the observation period, which may reflect the absence of inorganic bone-matrix components or additional osteoconductive cues in the current hydrogel system. More broadly, these findings position cellular contractility as an engineerable physical state for guiding osteovascular organoid maturation. Matrix design should therefore focus not only on providing permissive space or transport capacity, but also on tuning the contractile state of embedded multicellular constructs through physical parameters such as pore structure, matrix stiffness, and matrix remodeling properties. By modulating cellular contractility within an appropriate range, organoid-forming materials may more effectively coordinate cell differentiation, multicellular organization and metabolic function. This principle may guide the development of vascularized bone grafts, pre-vascularized spheroid constructs and organoid-laden hydrogels in which structural maturation and metabolic cooperation need to occur together. Several limitations should also be considered. First, cellular contractility within hydrogel-embedded spheroids was not directly quantified by force-based measurements, because traction force microscopy and related approaches remain technically challenging in 3D hydrogel systems. Second, although Laconic-NLS imaging supports lactate-mediated metabolic coupling, isotope tracing would more directly resolve carbon flux between ECs and MSCs. Overall, by linking hydrogel pore structure, cellular contractility, and intercellular metabolism, this study provides a framework for engineering osteovascular organoids with coordinated structural and metabolic maturation.

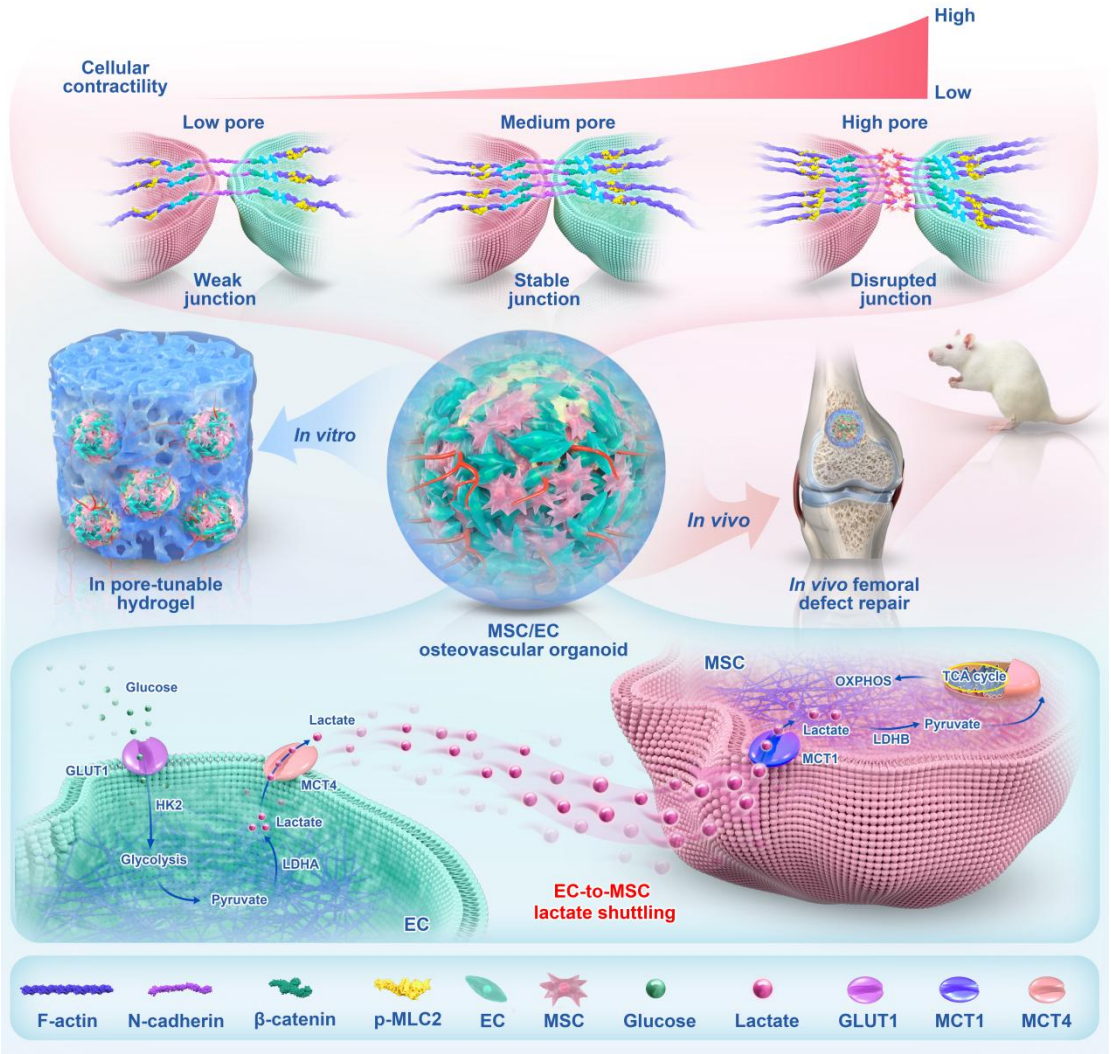


Fig. 6 | Pore-regulated cellular contractility coordinates osteovascular organoid maturation and lactate shuttling

Schematic illustration of cellular contractility-guided osteovascular organoid maturation, metabolic reprogramming and EC-to-MSC lactate shuttling. Hydrogel pore structure regulates cellular contractility and junctional organization, with intermediate contractility supporting stable MSC–EC interactions and osteovascular organoid maturation. Glycolytic ECs export lactate through MCT4, whereas MSCs take up lactate through MCT1 to support oxidative metabolism. This coordinated structural and metabolic maturation contributes to enhanced femoral defect repair.

Conclusion

Overall, this study demonstrates that pore-regulated cellular contractility coordinates multicellular organization and EC-to-MSC lactate shuttling to promote osteovascular organoid maturation and bone repair. By linking matrix pore design, cellular contractility, and intercellular metabolism, this work provides a framework for engineering osteovascular organoids in which structural and metabolic maturation can be achieved in parallel.

3. Methods

3.1. Fabrication and characterization of pore-tunable GelMA hydrogels

Pore-tunable hydrogels were prepared through polyethylene oxide (PEO)-induced liquid-liquid phase separation[29,30,60]. GelMA (Mw = 150 kDa, degree of substitution = 60%; EFL-GM-60, EFL Inc., Suzhou, China), PEO (Mw = 300 kDa; 182001, Sigma, St. Louis, MO, USA), and lithium phenyl-2,4,6-trimethylbenzoylphosphinate (LAP; EFL-LAP, EFL Inc.) were dissolved in sterile phosphate-buffered saline (PBS; Gibco, Thermo Fisher Scientific, Waltham, MA, USA) to generate NP, LP, MP, and HP precursor solutions with GelMA/PEO/LAP mass ratios of 100/0/5.5, 100/5/5.5, 100/15/5.5, and 100/30/5.5, respectively. The precursor solutions were stirred at 37 °C, protected from light until completely dissolved, and filtered through a 0.22 μm sterile syringe filter before use. The solutions were cast into cylindrical moulds and photocrosslinked using a 405 nm light source for 1 min. After crosslinking, the hydrogels were immersed in PBS or culture medium to remove PEO-rich droplets, thereby generating interconnected micropores within the GelMA network.

3.2. Scanning electron microscopy (SEM)

Hydrogel samples were rinsed with PBS, rapidly snap-frozen in liquid nitrogen, and lyophilized. The freeze-dried hydrogels were fractured to expose internal cross-sections and mounted on conductive adhesive tabs. Samples were sputter-coated with gold and imaged using a field-emission scanning electron microscope (GeminiSEM 300, ZEISS, Oberkochen, Germany) at an accelerating voltage of 5 kV. Pore diameters were quantified from SEM images using ImageJ software (National Institutes of Health, Bethesda, MD, USA).

3.3. Three-dimensional (3D) fluorescence reconstruction

To visualize the interconnected pore network in three dimensions, hydrogels were labelled with Alkene-Coupling Hydrogel Fluorescent Dye (EFL-DYE-UF-ENE-R, EFL Inc.) according to the manufacturer's instructions. Fluorescence images were acquired using a confocal microscope (STELLARIS 8, Leica, Wetzlar, Germany). Z-stack images were collected at 2 μm intervals and reconstructed using LAS X software (version 3.5, Leica).

3.4. Rheological characterization

Rheological properties of NP, LP, MP, and HP hydrogels were measured using a rotational rheometer (MARS 40, HAAKE, Germany) with parallel-plate geometry at a 1.0 mm gap and 25 °C. Strain-sweep tests were performed at 6.28 rad/s over 0.1–1000% strain. Time-sweep tests were conducted at 6.28 rad/s and 1% strain for 3600 s. Frequency-sweep tests were performed at 1% strain over 0.1–100 rad/s. Storage modulus (G′) and loss modulus (G″) were

recorded.

3.5. Compression testing

The bulk compressive properties of NP, LP, MP, and HP hydrogels were evaluated using a dynamic mechanical analyser (DMA 303, NETZSCH, Germany). Cylindrical hydrogel specimens with a diameter of 12 mm were prepared for testing. Uniaxial compression tests were performed at a constant loading rate of 0.5 mm/min with a preload of 1 N, and stress-strain curves were recorded in real time until a compression displacement of 2 mm was reached. The compressive modulus was calculated from the slope of the stress-strain curve within the 0-10% strain region.

3.6. Young's modulus analysis

Young's modulus of NP, LP, MP, and HP hydrogels was measured under hydrated conditions using a nanoindenter (Piuma, Optics11, Netherlands). Samples were immobilized in PBS during testing. Indentation was performed in displacement-control mode using a spherical probe with a spring constant of 0.530 N/m and a tip radius of 25 μm. Each cycle included loading to 12 μm for 1 s, holding for 1 s, and unloading for 1 s. Young's modulus was calculated from force-displacement curves using the Hertz contact model with a Poisson's ratio of 0.5 in Piuma software (version 3.5.0, Optics11).

3.7. Swelling and degradation assays

To evaluate swelling behaviour, cylindrical hydrogels (10 mm in diameter and 3 mm in height)

with different pore sizes were immersed in 5 mL PBS and incubated at 37 °C. At predetermined time points, samples were removed, gently blotted to eliminate surface-adsorbed liquid, and immediately weighed. The swelling ratio was calculated as follows:

$$\text{Swelling ratio } (\%) = \frac{W_1 - W_0}{W_0} \times 100\% \qquad (1)$$

where W_0 is the initial mass of the hydrogel, and W_1 is the mass at a given swelling time point.

To evaluate degradation behaviour, cylindrical hydrogels (10 mm in diameter and 3 mm in height) were incubated in 5 mL PBS at 37 °C in a constant-temperature shaking incubator. At predetermined time points over 1–8 weeks, samples were retrieved, gently blotted to remove surface moisture, and weighed. The degradation rate was calculated as follows:

$$\text{Degradation rate } (\%) = \frac{W_0 - W_t}{W_0} \times 100\% \qquad (2)$$

where W_0 is the initial mass of the hydrogel, and W_t is the mass of the hydrogel at time t.

3.8. FITC-dextran diffusion and permeability assay

Hydrogel transport properties were evaluated using FITC-dextran (Mw = 4 kDa; Sigma). For fluorescence imaging, hydrogels were incubated with 100 μg/mL FITC-dextran for 24 h and imaged under identical settings using a confocal microscope (STELLARIS 8, Leica). Pore-associated fluorescence intensity was quantified to assess tracer-accessible void space. For permeability analysis, FITC-dextran solution was added to the upper chamber of hydrogel-containing inserts, with PBS in the lower chamber as the receiving solution. At predetermined time points, the receiving solution was collected and replaced with fresh PBS. Fluorescence intensity was measured using a Varioskan LUX Multimode Microplate Reader (Thermo Fisher

610 Scientific) at 490/520 nm excitation/emission wavelengths. The permeability rate was
611 calculated according to a previous study as follows[61]:

612 $$\text{Permeability rate } (\%) = \frac{C_{lower} \times V_{lower}}{C_{initial} \times V_{added}} \times 100\% \qquad (3)$$

613 where C_{lower} and V_{lower} are the FITC-dextran concentration and volume of the receiving solution
614 collected from the lower chamber, respectively, and $C_{initial}$ and $V_{initial}$ are the initial concentration
615 and volume of FITC-dextran solution added to the upper chamber, respectively.

616

617 ***3.9. Spheroid preparation, hydrogel encapsulation, and osteovascular induction***

618 hBMSCs, HUVECs, and rBMSCs were purchased from ScienCell Research Laboratory
619 (Carlsbad, CA, USA). RUVECs were purchased from iCell Bioscience Inc. (Shanghai, China).
620 hBMSCs and rBMSCs were cultured in control medium consisting of α-MEM (Gibco), 10% fetal
621 bovine serum (Gibco), and 1% penicillin-streptomycin (Gibco). HUVECs and RUVECs were
622 maintained in standard endothelial cell medium (1001, ScienCell; iCell-e004-002r, iCell
623 Bioscience Inc., respectively). All cells were cultured at 37 °C with 5% CO_2, and passages 5–7
624 were used. Before spheroid assembly, hBMSCs and HUVECs were transduced with lentiviral
625 vectors encoding mCherry and EGFP, respectively, to enable lineage tracing and fluorescence-
626 activated cell sorting.

627

628 For *in vitro* osteovascular organoid experiments, mCherry-labelled hBMSCs and EGFP-
629 labelled HUVECs were mixed at a 1:1 ratio and assembled into osteovascular spheroids using
630 a Cell Spheroids Culture plate 96U well Kit (EFL-SP101, EFL Inc.). For ratio optimization,
631 hBMSC:HUVEC ratios of 3:1, 1:1, and 1:3 were compared, and HUVEC-only and hBMSC-only

spheroids were generated using the same approach. For rat femoral defect experiments, rBMSCs and RUVECs were assembled into osteovascular spheroids at a 1:1 ratio as above. Each spheroid contained 1000 cells. After spheroid formation for 48 h, spheroids were collected and gently suspended in hydrogel precursor solutions at a density of 5000 spheroids/mL. The spheroid-containing precursor solutions were then photocrosslinked to encapsulate spheroids within the NP, LP, MP, or HP hydrogels. After encapsulation, spheroid-laden hydrogels were maintained in a 1:1 mixture of control medium and endothelial cell medium for 24 h. For osteovascular induction, the culture medium was replaced with a 1:1 mixture of osteogenic medium and endothelial cell medium. The osteogenic medium consisted of control medium supplemented with 50 μg/mL ascorbic acid (Sigma), 10 mM β-glycerophosphate (Sigma), and 10 nM dexamethasone (Sigma).

3.10. Cell viability and spheroid sprouting assay

For viability analysis, samples were rinsed with PBS and incubated with Calcein-AM/propidium iodide live/dead staining solution (KGA9501-100, KeyGEN BioTECH, Nanjing, China) according to the manufacturer's protocol. Fluorescence images were acquired using a confocal microscope (STELLARIS 8, Leica) under identical imaging settings. Spheroid sprouting was monitored by bright-field imaging and Calcein-AM fluorescence imaging at the indicated time points. Sprouting morphology was quantified using ImageJ and AngioTool software (version 0.6a, National Institutes of Health, Bethesda, MD, USA)[62].

3.11. Animals

6-week-old male nude mice and 8-week-old male Sprague-Dawley rats were purchased from Vital River Laboratory Animal Technology Co., Ltd. (Beijing, China). All animal procedures were performed in accordance with the ethical standards of the Institutional Animal Care and Use Committee of the Peking University Health Science Center (Approved Number: DLASBD0248). For ectopic ossification analysis, LP, MP, and HP osteovascular organoid constructs were implanted subcutaneously into nude mice and harvested after 4 weeks. For bone defect repair, femoral defects were established in Sprague-Dawley rats. Rats were anesthetized with isoflurane, and the femoral condyles were exposed through skin incisions followed by blunt dissection of the surrounding muscles. A cylindrical defect with a diameter of 3.0 mm and a depth of 2.0 mm was generated in the femoral condyle using an electric drill. LP, MP, and HP osteovascular organoid constructs were implanted into the defects, while untreated defects served as the blank control. Samples were harvested after 8 weeks for downstream experiments.

3.12. Micro-computed tomography (micro-CT)

Samples were fixed in 4% paraformaldehyde (Servicebio) before micro-CT scanning. Micro-CT analysis was performed using a VNC-102 micro-CT system (Pingseng Healthcare Technology, China) at 90 kV and 80 μA. The scanning precision was 10 μm for ectopic ossification samples and 30 μm for rat femoral defect samples. 3D reconstruction and bone morphometric analysis were performed using the accompanying analysis software. BMD, BV/TV, Tb.Th, and Tb.N were calculated within the implanted or defect region.

3.13. Histological, immunofluorescence, and immunohistochemical analyses of in vivo samples

Animal samples were processed according to the sample type. For ectopic ossification analysis, harvested implants were fixed in 4% paraformaldehyde (Servicebio) and embedded in optimal cutting temperature compound for frozen sectioning. For rat femoral defect samples, specimens were fixed, decalcified in 10% ethylenediaminetetraacetic acid (EDTA; Servicebio), dehydrated, embedded in paraffin, and sectioned into 5-μm-thick slices. Major organs were fixed, paraffin-embedded, and sectioned for biosafety evaluation. Histological staining, including hematoxylin and eosin (H&E), Masson's trichrome, and Alizarin Red S staining, was performed according to standard protocols. Alizarin Red S staining was performed using an osteogenesis staining kit (Beyotime, Shanghai, China).

For immunofluorescence staining, sections were blocked and incubated with primary antibodies against the indicated markers, including rabbit anti-OCN antibody (23418-1-AP, Proteintech, Wuhan, China; 1:500), rabbit anti-RUNX2 antibody (20700-1-AP, Proteintech; 1:500), mouse anti-VEGFA antibody (66828-1-Ig, Proteintech; 1:500), rabbit anti-CD31 antibody (11265-1-AP, Proteintech; 1:250), and mouse anti-α-SMA antibody (67735-1-Ig, Proteintech; 1:500), followed by the corresponding fluorescent secondary antibodies (Proteintech; 1:600). Nuclei were counterstained with 4′,6-diamidino-2-phenylindole (DAPI; D9542, Sigma; 1:100). For immunohistochemistry of femoral defect samples, paraffin sections were deparaffinized, rehydrated, subjected to antigen retrieval, blocked, and incubated with rabbit anti-OCN antibody (23418-1-AP, Proteintech; 1:250), followed by horseradish peroxidase-conjugated

secondary antibody (RGAR011, Proteintech) and chromogenic detection. Images were acquired using a Pannoramic SCAN II digital slide scanner (3DHISTECH, Budapest, Hungary), and staining intensity was quantified using ImageJ software where applicable.

3.14. Immunostaining and image analysis of organoids

Samples were fixed with 4 % paraformaldehyde (Servicebio) for 15 min at room temperature, washed with PBS, and permeabilized with 0.1% Triton X-100 (Beyotime) for 10 min. After blocking with 5 % bovine serum albumin (Beyotime) for 1 h, samples were incubated with primary antibodies against the indicated markers, including Rabbit anti-RUNX2 antibody (ab192256, Abcam, Cambridge, UK; 1:1000), Rabbit anti-CD31 antibody(11265-1-AP, Proteintech; 1:250), Rabbit anti-PDGFR-β antibody (3169T, Cell Signaling Technology, Danvers, MA, USA; 1:250), Rabbit anti-APLN antibody (ab59469, Abcam; 1:250), Rabbit anti-p-MLC2 antibody (95777T, Cell Signaling Technology; 1:600), Rabbit anti-N-cadherin (ab18203, Abcam; 1:200), Rabbit-anti-β-catenin antibody (8480, Cell Signaling Technology; 1:250), Rabbit-anti-VE-cadherin antibody (83766-2-RR, Proteintech; 1:400), Rabbit anti-MCT1 antibody (20139-1-AP, Proteintech; 1:250), and Rabbit anti-MCT4 antibody (22787-1-AP, Proteintech; 1:500), overnight at 4 °C. After washing, samples were incubated with the corresponding fluorescent secondary antibodies (RGAR005, Proteintech; 1:600) for 2 h at room temperature. F-actin and nuclei were stained with Alexa Fluor 594 phalloidin (PF00003, Proteintech; 1:400) and DAPI (D9542, Sigma; 1:100), respectively, where indicated. Images were acquired using a confocal microscope (STELLARIS 8, Leica) under identical acquisition settings for each staining experiment. Fluorescence intensity was quantified using ImageJ software. For cell-type-specific

analysis, mCherry-labelled hBMSCs and EGFP-labelled HUVECs were used to define lineage-specific regions or cell populations when applicable.

3.15. Quantitative real-time PCR (qPCR)

Total RNA was extracted from isolated cells following the manufacturer's instructions using a total RNA isolation kit (RC112-01, Vazyme, Nanjing, China). After reverse transcription to cDNA, qPCR was carried out with SYBR qPCR Master Mix (Q712-02, Vazyme) using the CFX96 Real-Time System (Bio-Rad, Hercules, CA, USA). The endogenous control for normalizing gene expression was determined by assessing the level of *GAPDH*. The primer sequences used are listed in **Supplementary Table 1**.

3.16. RNA sequencing (RNA-seq)

RNA-seq and bioinformatic analyses were performed by OE Biotech Co., Ltd. (Shanghai, China). Briefly, cells were isolated from LP, MP, and HP groups, and total RNA was extracted using TRIzol reagent (Invitrogen, Thermo Fisher Scientific). RNA purity, concentration, and integrity were assessed before library construction. Sequencing libraries were prepared using a VAHTS Universal V10 RNA-seq Library Prep Kit (Vazyme) according to the manufacturer’s instructions and sequenced on an Illumina sequencing platform.

After quality control and adaptor trimming, clean reads were aligned to the human reference genome. Differentially expressed genes between groups were identified using the DESeq2 package in R software (version 4.4.3; R Foundation for Statistical Computing, Vienna, Austria),

with |log2 fold change| > 0.58 and $P < 0.05$ used as the screening threshold. PCA, heatmap visualization, GO enrichment analysis, KEGG pathway enrichment analysis, and GSEA were performed using R software.

3.17. Pharmacological modulation of contractility and metabolism

Pharmacological treatments were performed to modulate cellular contractility, glycolysis, mitochondrial oxidative phosphorylation, and lactate availability. To reduce cellular contractility, different groups were treated with 30 μM Y-27632 (S1049, Selleck Chemicals, Houston, TX, USA), a ROCK inhibitor, for 24 h. To enhance myosin-dependent contractility, organoids were treated with 100 nM Calyculin A (208851, Sigma) for 24 h before downstream analyses. To perturb metabolic activity, the MP group was treated with 5 mM 2-DG (S4701, Selleck Chemicals) for 24 h to inhibit glycolysis or with 1 μM oligomycin (MCH32, Selleck Chemicals) for 24 h to inhibit ATP synthase-dependent mitochondrial oxidative phosphorylation. For lactate-rescue experiments, exogenous L-lactate was supplemented at 10 mM for 24 h before subsequent analyses.

3.18. Fluorescence lifetime imaging microscopy (FLIM)-based membrane tension measurement

Membrane tension was assessed using FLIM[63]. Organoids in different groups were incubated with 1 μM Flipper-TR (CY-SC020, Cytoskeleton, Inc., Denver, CO, USA) at 37 °C for 30 min before imaging. Samples were imaged using a FLIM-compatible confocal microscope (STELLARIS 8, Leica) with 488 nm excitation and 575–625 nm emission collection.

Fluorescence lifetime values were extracted from regions of interest defined along the cell membrane, and relative membrane tension was calculated after normalization to the indicated control group.

3.19. Untargeted liquid chromatography-mass spectrometry (LC-MS)-based Metabolomics

Untargeted LC-MS-based metabolomic profiling was performed by OE Biotech Co., Ltd. Cells were collected from LP, MP, and HP groups and rapidly processed for metabolite extraction. Metabolites were extracted using cold organic solvent containing an internal standard according to the service provider's standard protocol. Quality-control samples were prepared by pooling equal aliquots from all samples to monitor analytical reproducibility.

Metabolomic data were acquired using an ACQUITY UPLC I-Class Plus system (Waters Corporation, Milford, MA, USA) coupled to a Q Exactive mass spectrometer equipped with a heated electrospray ionization source (Thermo Fisher Scientific). Chromatographic separation was performed using an ACQUITY UPLC HSS T3 column (1.8 μm, 2.1 × 100 mm) in both positive and negative ion modes. Raw data were processed for peak detection, alignment, normalization, and metabolite annotation. Differential metabolites were screened using Variable Importance in Projection > 1.0 and $P < 0.05$ as the threshold. Differential metabolites were subjected to KEGG pathway enrichment analysis and further integrated with RNA-seq data to identify pathways altered at both transcriptional and metabolite levels.

3.20. Fluorescence-activated cell sorting (FACS)

For experiments requiring isolated cells, organoids containing GFP-labelled HUVECs and mCherry-labelled hBMSCs were dissociated into single-cell suspensions using GelMA lysis solution (EFL-GM-LS-001, EFL Inc.) together with enzymatic digestion by trypsin (Gibco). The resulting cell suspensions were gently pipetted, filtered through a cell strainer, and subjected to FACS using a BD FACS Symphony S6 cell sorter (BD Biosciences, Franklin Lakes, NJ, USA). Cells were first gated according to forward scatter and side scatter to exclude debris, followed by doublet exclusion using FSC-A/FSC-H and dead-cell exclusion. GFP-positive HUVECs and mCherry-positive hBMSCs were sorted according to FITC-A and PE-A fluorescence signals, respectively. Sorted cells were collected for downstream experiments.

3.21. Seahorse metabolic flux analysis

After osteovascular organoids were cultured *in vitro* for 14 days, EGFP-labelled HUVECs and mCherry-labelled hBMSCs were isolated by fluorescence-activated cell sorting as described above. Sorted cells were seeded into Seahorse XFe96 cell culture microplates (Agilent Technologies, Santa Clara, CA, USA) at a density of 15000 cells per well and allowed to attach overnight. One hour before the assay, cells were washed with Seahorse XF assay medium (Agilent Technologies) and incubated at 37 °C in a non-CO_2 incubator. Oxygen consumption rate (OCR) and extracellular acidification rate (ECAR) were measured using a Seahorse XFe96 Extracellular Flux Analyzer (Agilent Technologies), and metabolic parameters were quantified using Wave software (version 2.6, Agilent Technologies).

For mitochondrial stress analysis, sorted hBMSCs were sequentially treated with 1.5 μM oligomycin (ab141829, Abcam), 1 μM carbonyl cyanide-4-(trifluoromethoxy)phenylhydrazone (FCCP; M9051, AbMole BioScience, Houston, TX, USA), and 0.5 μM rotenone (M6209, AbMole BioScience)/antimycin A (GC49360, GLPBIO, Montclair, CA, USA). Basal respiration, maximal respiration, and spare respiratory capacity were calculated from OCR profiles. For glycolysis stress analysis, sorted HUVECs were sequentially treated with 10 mM glucose (103577, Agilent Technologies), 1 μM oligomycin (ab141829, Abcam), and 50 mM 2-DG (HY-13966, MedChemExpress, Monmouth Junction, NJ, USA). Glycolysis, glycolytic capacity, and glycolytic reserve were calculated from ECAR profiles. All values were normalized to cell number.

3.22. Lentiviral transduction

Lentiviral transduction was used for lineage tracing, lactate imaging, and contractility perturbation. hBMSCs and HUVECs were transduced with mCherry- and EGFP-encoding lentiviruses, respectively. hBMSCs were transduced with Laconic-NLS for intracellular lactate imaging. For contractility perturbation, HUVECs were transduced with MYL9-targeting shRNA or non-targeting control shRNA, whereas hBMSCs were transduced with a phosphomimetic MLC2 (T18D/S19D) overexpression construct or empty-vector control. All lentiviral vectors were designed and purchased from Hanbio Biotechnology Co., Ltd. (Shanghai, China).

Briefly, cells at approximately 70% confluence were incubated with lentiviral particles and 8 μg/mL polybrene for 24 h, followed by medium replacement and 48 h of culture. Stable shRNA-

or overexpression-modified cells were selected with 2 μg/mL puromycin for 72 h and maintained with 1 μg/mL puromycin before downstream experiments. Detailed construct information is provided in **Supplementary Table 2**.

3.23. Laconic-NLS fluorescence resonance energy transfer (FRET) imaging

To evaluate intracellular lactate dynamics, Laconic-NLS-transduced hBMSCs were incorporated into spheroids and cultured under different treatment conditions for 7 days before imaging[64]. FRET imaging was performed using a confocal microscope (STELLARIS 8, Leica) under identical acquisition settings. Upon excitation at 405 nm, mTFP fluorescence was collected at 455–495 nm, while mVenus fluorescence was collected at 514–560 nm. After background subtraction, the mTFP/mVenus fluorescence intensity ratio was calculated as a relative readout of intracellular lactate levels.

3.24. Extracellular lactate measurement

Culture supernatants were collected at the indicated time points and analyzed using an L-lactate assay kit (S0208S, Beyotime). Lactate concentrations were calculated from a standard curve.

3.25. Statistical analyses

All data are presented as mean ± SD. Statistical analyses were performed using Prism software (version 10.2.3, GraphPad Software, Boston, MA, USA). For comparisons between two groups, a two-sided Student's t-test was used. For comparisons among more than two groups, one-

way analysis of variance (ANOVA) followed by Tukey's post-hoc test was applied. $P < 0.05$ was considered statistically significant. Exact P values and sample sizes (n) are provided in the corresponding figures and figure legends.

Funding

This work was supported by the National Natural Science Foundation of China (grant number 82271032, 82470943, 82401061), Hainan Provincial Natural Science Foundation of China (grant number 825YXQN602), Joint Program on Health Science & Technology Innovation of Hainan Province (grant number WSJK2025ZD210), Peking University Clinical Scientist Training Program, supported by "the Fundamental Research Funds for the Central Universities" (grant number BMU2025PYJH011), Clinical Medicine Plus X-Young Scholars Project, Peking University, the Fundamental Research Funds for the Central Universities (grant number PKU2026PKULCXQ012)

Author contributions

Zhanqi Wang: Writing – Original draft, Visualization. Zhuqing Wan: Data curation. Dongdong Huang, Yicheng Yang: Methodology, Formal analysis. Jundan Yi, Xiaoqiang Bai: Investigation. Yangkun Liu, Mingchu Zhao, Xiaodong Guo: Software. Yongsheng Zhou: Project administration, Funding acquisition. Longwei Lv: Supervision, Writing – review & editing, Funding acquisition.

Declaration of Competing Interest

The authors declare no competing interests.

Data availability

The untargeted LC–MS metabolomics data generated in this study have been deposited in the MetaboLights repository under accession code MTBLS16066. Source data are provided with this paper.

References

1 Hofer, M. & Lutolf, M. P. Engineering organoids. *Nature reviews. Materials* **6**, 402-420, doi:10.1038/s41578-021-00279-y (2021).

2 Zhao, Z. et al. Organoids. *Nature Reviews Methods Primers* **2**, 94, doi:10.1038/s43586-022-00174-y (2022).

3 Kim, J., Koo, B. K. & Knoblich, J. A. Human organoids: model systems for human biology and medicine. *Nature reviews. Molecular cell biology* **21**, 571-584, doi:10.1038/s41580-020-0259-3 (2020).

4 Quintard, C. *et al.* A microfluidic platform integrating functional vascularized organoids-on-chip. *Nature communications* **15**, 1452, doi:10.1038/s41467-024-45710-4 (2024).

5 Grebenyuk, S. *et al.* Large-scale perfused tissues via synthetic 3D soft microfluidics. *Nature communications* **14**, 193, doi:10.1038/s41467-022-35619-1 (2023).

6 Skylar-Scott, M. A. *et al.* Orthogonally induced differentiation of stem cells for the programmatic patterning of vascularized organoids and bioprinted tissues. *Nature biomedical engineering* **6**, 449-462, doi:10.1038/s41551-022-00856-8 (2022).

7 Frenz-Wiessner, S. *et al.* Generation of complex bone marrow organoids from human induced pluripotent stem cells. *Nature methods* **21**, 868-881, doi:10.1038/s41592-024-02172-2 (2024).

8 Kim, M. H. *et al.* High-throughput bioprinting of spheroids for scalable tissue fabrication. *Nature communications* **15**, 10083, doi:10.1038/s41467-024-54504-7 (2024).

9 Blatchley, M. R. & Anseth, K. S. Middle-out methods for spatiotemporal tissue engineering of organoids. *Nature reviews bioengineering* **1**, 329-345, doi:10.1038/s44222-023-00039-3 (2023).

10 Kim, D. et al. From organoid culture to manufacturing: technologies for reproducible and scalable organoid production. *npj Biomedical Innovations* **3**, 12, doi:10.1038/s44385-025-00054-6 (2026).

11 Huang, M. S., Christakopoulos, F., Roth, J. G. & Heilshorn, S. C. Organoid bioprinting: from cells to functional tissues. *Nature Reviews Bioengineering* **3**, 126–142, doi:10.1038/s44222-024-00268-0 (2025).

12 Chaudhuri, O., Cooper-White, J., Janmey, P. A., Mooney, D. J. & Shenoy, V. B. Effects of extracellular matrix viscoelasticity on cellular behaviour. *Nature* **584**, 535-546, doi:10.1038/s41586-020-2612-2 (2020).

13 Saraswathibhatla, A., Indana, D. & Chaudhuri, O. Cell-extracellular matrix

mechanotransduction in 3D. *Nature reviews. Molecular cell biology* **24**, 495-516, doi:10.1038/s41580-023-00583-1 (2023).

14 Mao, Y. & Wickström, S. A. Mechanical state transitions in the regulation of tissue form and function. *Nature reviews. Molecular cell biology* **25**, 654-670, doi:10.1038/s41580-024-00719-x (2024).

15 Pérez-González, C. *et al.* Mechanical compartmentalization of the intestinal organoid enables crypt folding and collective cell migration. *Nature cell biology* **23**, 745-757, doi:10.1038/s41556-021-00699-6 (2021).

16 Zhou, D. W. *et al.* Force-FAK signaling coupling at individual focal adhesions coordinates mechanosensing and microtissue repair. *Nature communications* **12**, 2359, doi:10.1038/s41467-021-22602-5 (2021).

17 Cai, Y. *et al.* Cytoskeletal coherence requires myosin-IIA contractility. *Journal of cell science* **123**, 413-423, doi:10.1242/jcs.058297 (2010).

18 Kim, J. *et al.* Stress-induced plasticity of dynamic collagen networks. *Nature communications* **8**, 842, doi:10.1038/s41467-017-01011-7 (2017).

19 Meshel, A. S., Wei, Q., Adelstein, R. S. & Sheetz, M. P. Basic mechanism of three-dimensional collagen fibre transport by fibroblasts. *Nature cell biology* **7**, 157-164, doi:10.1038/ncb1216 (2005).

20 Gjorevski, N., Piotrowski, A. S., Varner, V. D. & Nelson, C. M. Dynamic tensile forces drive collective cell migration through three-dimensional extracellular matrices. *Scientific reports* **5**, 11458, doi:10.1038/srep11458 (2015).

21 McEvoy, E. *et al.* Feedback between mechanosensitive signaling and active forces governs endothelial junction integrity. *Nature communications* **13**, 7089, doi:10.1038/s41467-022-34701-y (2022).

22 Liu, Z. *et al.* Mechanical tugging force regulates the size of cell-cell junctions. *Proceedings of the National Academy of Sciences of the United States of America* **107**, 9944-9949, doi:10.1073/pnas.0914547107 (2010).

23 Engl, W., Arasi, B., Yap, L. L., Thiery, J. P. & Viasnoff, V. Actin dynamics modulate mechanosensitive immobilization of E-cadherin at adherens junctions. *Nature cell biology* **16**, 587-594, doi:10.1038/ncb2973 (2014).

24 Founounou, N. *et al.* Tissue fluidity mediated by adherens junction dynamics promotes planar cell polarity-driven ommatidial rotation. *Nature communications* **12**, 6974, doi:10.1038/s41467-021-27253-0 (2021).

25 Urbanska, M. & Guck, J. Single-Cell Mechanics: Structural Determinants and Functional Relevance. *Annual review of biophysics* **53**, 367-395, doi:10.1146/annurev-biophys-030822-030629 (2024).

26 Polz, M. *et al.* Cellular Responses to Mechanical Cues Across Scales: From Fundamental Insights to Translational Potential. *Advanced healthcare materials*, e71400, doi:10.1002/adhm.71400 (2026).

27 Sun, D. *et al.* Matrix Viscoelasticity Controls Differentiation of Human Blood Vessel Organoids into Arterioles and Promotes Neovascularization in Myocardial Infarction. *Advanced materials (Deerfield Beach, Fla.)* **37**, e2410802, doi:10.1002/adma.202410802 (2025).

28 Wei, Z. *et al.* Hydrogels with tunable mechanical plasticity regulate endothelial cell

outgrowth in vasculogenesis and angiogenesis. *Nature communications* **14**, 8307, doi:10.1038/s41467-023-43768-0 (2023).

29 Ying, G. L. *et al.* Aqueous Two-Phase Emulsion Bioink-Enabled 3D Bioprinting of Porous Hydrogels. *Advanced materials (Deerfield Beach, Fla.)* **30**, e1805460, doi:10.1002/adma.201805460 (2018).

30 Mu, J. *et al.* Phase-separated hydrogels for advanced biomedical engineering: From material design to applications. *Materials today. Bio* **38**, 103096, doi:10.1016/j.mtbio.2026.103096 (2026).

31 Cao, H., Duan, L., Zhang, Y., Cao, J. & Zhang, K. Current hydrogel advances in physicochemical and biological response-driven biomedical application diversity. *Signal transduction and targeted therapy* **6**, 426, doi:10.1038/s41392-021-00830-x (2021).

32 Jiang, S. *et al.* Cryoprotectant enables structural control of porous scaffolds for exploration of cellular mechano-responsiveness in 3D. *Nature communications* **10**, 3491, doi:10.1038/s41467-019-11397-1 (2019).

33 Zauchner, D. *et al.* Synthetic biodegradable microporous hydrogels for in vitro 3D culture of functional human bone cell networks. *Nature communications* **15**, 5027, doi:10.1038/s41467-024-49280-3 (2024).

34 Müller, M. Z. *et al.* Cell-guiding microporous hydrogels by photopolymerization-induced phase separation. *Nature communications* **16**, 4923, doi:10.1038/s41467-025-60113-9 (2025).

35 Wu, D. *et al.* Single-cell metabolic imaging reveals a SLC2A3-dependent glycolytic burst in motile endothelial cells. *Nature metabolism* **3**, 714-727, doi:10.1038/s42255-021-00390-y (2021).

36 Leung, S. W. S. & Shi, Y. The glycolytic process in endothelial cells and its implications. *Acta pharmacologica Sinica* **43**, 251-259, doi:10.1038/s41401-021-00647-y (2022).

37 Lin, C. *et al.* Impaired mitochondrial oxidative metabolism in skeletal progenitor cells leads to musculoskeletal disintegration. *Nature communications* **13**, 6869, doi:10.1038/s41467-022-34694-8 (2022).

38 Quarato, E. R. *et al.* Efferocytosis by bone marrow mesenchymal stromal cells disrupts osteoblastic differentiation via mitochondrial remodeling. *Cell death & disease* **14**, 428, doi:10.1038/s41419-023-05931-9 (2023).

39 Chen, J. & Jiang, X. Sirtuin 5-mediated desuccinylation of Slc25a4 inhibits osteoporosis by enhancing mitochondrial respiration. *Bone research* **13**, 93, doi:10.1038/s41413-025-00464-7 (2025).

40 Bertels, J. C., He, G. & Long, F. Metabolic reprogramming in skeletal cell differentiation. *Bone research* **12**, 57, doi:10.1038/s41413-024-00374-0 (2024).

41 Brooks, G. A. *et al.* Tracing the lactate shuttle to the mitochondrial reticulum. *Experimental & molecular medicine* **54**, 1332-1347, doi:10.1038/s12276-022-00802-3 (2022).

42 Zhang, D. *et al.* Metabolic regulation of gene expression by histone lactylation. *Nature* **574**, 575-580, doi:10.1038/s41586-019-1678-1 (2019).

43 Dimmer, K. S., Friedrich, B., Lang, F., Deitmer, J. W. & Bröer, S. The low-affinity monocarboxylate transporter MCT4 is adapted to the export of lactate in highly

glycolytic cells. *The Biochemical journal* **350 Pt 1**, 219-227 (2000).
44 Payen, V. L., Mina, E., Van Hée, V. F., Porporato, P. E. & Sonveaux, P. Monocarboxylate transporters in cancer. *Molecular metabolism* **33**, 48-66, doi:10.1016/j.molmet.2019.07.006 (2020).
45 Lou, X. et al. Sequential angiogenic–osteogenic coupling via a spatiotemporally graded hydrogel enables vascularized bone organoids for critical-sized calvarial defect reconstruction. *Composites Part B: Engineering* **302,** 112553, doi:10.1016/j.compositesb.2025.112553 (2025).
46 Wu, Y. *et al.* Organoids in the oral and maxillofacial region: present and future. *International journal of oral science* **16**, 61, doi:10.1038/s41368-024-00324-w (2024).
47 de Janon, A. et al. Free-floating long-term vascularized mesenchymal organoids. *iScience* **29,** 114548, doi:10.1016/j.isci.2025.114548 (2026).
48 Malinova, T. S. *et al.* A junctional PACSIN2/EHD4/MICAL-L1 complex coordinates VE-cadherin trafficking for endothelial migration and angiogenesis. *Nature communications* **12**, 2610, doi:10.1038/s41467-021-22873-y (2021).
49 Salvi, A. M., Bays, J. L., Mackin, S. R., Mege, R. M. & DeMali, K. A. Ankyrin G organizes membrane components to promote coupling of cell mechanics and glucose uptake. *Nature cell biology* **23**, 457-466, doi:10.1038/s41556-021-00677-y (2021).
50 Nam, H., Yu, G., Ahn, S. I. & Nam, S. Mechanical regulation of metabolism, epigenetics, and their interplay. *npj Biomedical Innovations* **3,** 5, doi:10.1038/s44385-025-00059-1 (2026).
51 Zanotelli, M. R., Zhang, J. & Reinhart-King, C. A. Mechanoresponsive metabolism in cancer cell migration and metastasis. *Cell metabolism* **33**, 1307-1321, doi:10.1016/j.cmet.2021.04.002 (2021).
52 Zhang, J. *et al.* Endothelial Lactate Controls Muscle Regeneration from Ischemia by Inducing M2-like Macrophage Polarization. *Cell metabolism* **31**, 1136-1153.e1137, doi:10.1016/j.cmet.2020.05.004 (2020).
53 Chen, J. *et al.* Lactate and lactylation in cancer. *Signal transduction and targeted therapy* **10**, 38, doi:10.1038/s41392-024-02082-x (2025).
54 Wu, J. *et al.* Endothelial Cell-Derived Lactate Triggers Bone Mesenchymal Stem Cell Histone Lactylation to Attenuate Osteoporosis. *Advanced science (Weinheim, Baden-Wurttemberg, Germany)* **10**, e2301300, doi:10.1002/advs.202301300 (2023).
55 Mächler, P. *et al.* In Vivo Evidence for a Lactate Gradient from Astrocytes to Neurons. *Cell metabolism* **23**, 94-102, doi:10.1016/j.cmet.2015.10.010 (2016).
56 Shi, C. *et al.* MCT1-mediated endothelial cell lactate shuttle as a target for promoting axon regeneration after spinal cord injury. *Theranostics* **14**, 5662-5681, doi:10.7150/thno.96374 (2024).
57 Lee, H. W. *et al.* Endothelium-derived lactate is required for pericyte function and blood-brain barrier maintenance. *The EMBO journal* **41**, e109890, doi:10.15252/embj.2021109890 (2022).
58 Li, F. *et al.* Glial Metabolic Rewiring Promotes Axon Regeneration and Functional Recovery in the Central Nervous System. *Cell metabolism* **32**, 767-785.e767, doi:10.1016/j.cmet.2020.08.015 (2020).
59 Looser, Z. J. *et al.* Oligodendrocyte-axon metabolic coupling is mediated by

extracellular K(+) and maintains axonal health. *Nature neuroscience* **27**, 433-448, doi:10.1038/s41593-023-01558-3 (2024).

60 Wu, X. et al. Biomimetic porous hydrogel scaffolds enabled vascular ingrowth and osteogenic differentiation for vascularized tissue-engineered bone regeneration. *Applied Materials Today* **27,** 101478, doi:10.1016/j.apmt.2022.101478 (2022).

61 Ding, R. *et al.* The increase in the pore size of gelatin methacryloyl (GelMA) macroporous hydrogel promotes cell proliferation by enhancing substance permeability. *Biomaterials science* **14**, 1978-1995, doi:10.1039/d5bm01628b (2026).

62 Zudaire, E., Gambardella, L., Kurcz, C. & Vermeren, S. A computational tool for quantitative analysis of vascular networks. *PloS one* **6**, e27385, doi:10.1371/journal.pone.0027385 (2011).

63 Colom, A. *et al.* A fluorescent membrane tension probe. *Nature chemistry* **10**, 1118-1125, doi:10.1038/s41557-018-0127-3 (2018).

64 San Martín, A. *et al.* A genetically encoded FRET lactate sensor and its use to detect the Warburg effect in single cancer cells. *PloS one* **8**, e57712, doi:10.1371/journal.pone.0057712 (2013).

Supplementary Files

This is a list of supplementary files associated with this preprint. Click to download.

- FigSI71027.tif
- FigSI41027.tif
- FigSI51027.tif
- FigSI91027.tif
- FigSI81027.tif
- FigSI31027.tif
- FigSI61027.tif
- SupplementaryInformation20261028.docx
- FigSI11027.tif
- FigSI21027.tif